



Structural and activity comparison of self-limiting versus traditional Pt electro-depositions on nanopillar Ni films

Sonja A. Francis^a, Ryan T. Tucker^b, Michael J. Brett^{b,c}, Steven H. Bergens^{a,*}

^a Department of Chemistry, University of Alberta, Edmonton, Alberta T6G 2G2, Canada

^b Department of Electrical and Computer Engineering, University of Alberta, Edmonton, Alberta T6G 2V4, Canada

^c National Institute for Nanotechnology, 11421 Saskatchewan Drive NW, Edmonton, Alberta T6G 2M9, Canada

HIGHLIGHTS

- ▶ This is the first report of Pt–Ni glancing angle deposited (GLAD) based electrocatalysts.
- ▶ We contrast 2 methods to electro-deposit Pt on GLAD Ni nanopillars.
- ▶ We evaluate 2-propanol oxidation activity of the Pt–Ni deposits in alkaline media.
- ▶ Activity at low potentials results from the combined activity of Ni and Pt.
- ▶ At high potentials, Ni promotes Pt activity via a bifunctional effect.

ARTICLE INFO

Article history:

Received 12 July 2012

Received in revised form

6 September 2012

Accepted 8 September 2012

Available online 13 September 2012

Keywords:

Platinum

Nickel

Glancing angle deposition

2-Propanol

Alkaline

Direct alcohol fuel cell

ABSTRACT

We report the fabrication, characterisation, and electro-catalytic activity of $<0.3 \text{ mg cm}^{-2}$ platinum deposits onto $\sim 500 \text{ nm}$ long nickel nanopillar substrates (Ni_{NP}) synthesised by glancing angle deposition (GLAD). This is the first reported study of GLAD-based Pt–Ni electro-catalysts and the first alcohol oxidation study on any GLAD based electro-catalyst. The Pt was deposited onto Ni_{NP} via either 1) an unconventional, self-limiting, relatively high current density galvanostatic deposition, with a Pt counter electrode as the source of Pt, or 2) via a conventional potentiostatic deposition from Pt salts dissolved in acidic electrolytes. X-ray Diffraction (XRD) and Inductively Coupled Plasma Mass Spectrometry (ICP-MS) confirm the successful deposition of Pt onto Ni_{NP} , while Scanning Electron Microscopy (SEM) shows that the nanopillar morphology is preserved but the Pt morphology is significantly different between the two methods. The galvanostatic procedure resulted in a conformal Pt deposition over the entire surface of the Ni_{NP} . The conventional procedure appeared to be mass-transfer limited, with most of the Pt being deposited on the tops of the Ni_{NP} . Cyclic voltammetry in 1 M KOH shows an enhancement of the surface area of the catalysts upon Pt deposition and corroborates the presence of Pt on the Ni_{NP} surface. Both prepared catalysts show high electro-catalytic activity towards 2-propanol oxidation in the KOH electrolyte at 60°C . The activity enhancement below 300 mV vs. RHE (RHE = reversible hydrogen electrode) was attributed to the combined activity of the Pt and Ni components in the catalysts. At higher potentials, a bifunctional mechanism was suggested. Finally, a geometric/composition effect may be at work in the traditionally deposited catalyst, and requires further investigation.

© 2012 Elsevier B.V. All rights reserved.

1. Introduction

Alkaline Direct Alcohol Fuel Cells (ADAFCS) are being investigated as power sources for portable electronic devices for several reasons. Alcohols are readily available, liquid over wide temperature ranges [1], have promising electrochemical activity at

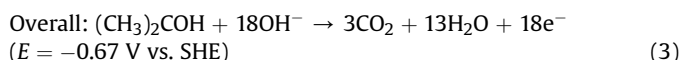
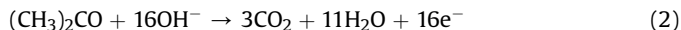
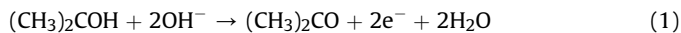
moderate temperatures [2], and have higher energy densities than hydrogen [3]. Alkaline systems are studied because the kinetics for both alcohol electro-oxidation and oxygen reduction are faster in base than they are in acid [3]. Methanol (MeOH) is the most studied alcohol fuel due to its ready availability and the absence of C–C bonds, making the complete oxidation of MeOH to CO_2 more facile than higher alcohols [4]. It is well known, however, that the electro-oxidation of MeOH self-poisons by CO or related intermediates that bind strongly to the catalyst surface. Further, the electro-oxidation of primary alcohols generates carboxylic acids or CO_2 as

* Corresponding author. Tel.: +1 780 492 9703; fax: +1 780 492 8231.

E-mail address: steve.bergens@ualberta.ca (S.H. Bergens).

products – species that consume the alkaline electrolyte unless they can be removed from the system. 2-Propanol (2-PrOH) is investigated as an alternative to MeOH in ADAFCs in part because 2-PrOH is less toxic [5] and its electro-oxidation onset potentials are lower over Pt and Pt–Ru catalysts [6,7]. Further, the two-electron oxidation of 2-PrOH is reversible in principle, leading to a rechargeable system [7].

The mechanism for the oxidation of 2-PrOH over Pt in base is potential dependent, as represented schematically by Equations (1) and (2) [8].



In the voltage range from ~ 50 to 250 mV vs. RHE (RHE = Reversible Hydrogen Electrode), the oxidation product is believed to be predominantly acetone (Equation (1)). This oxidation is substantially more facile than that of MeOH because the build-up of strongly adsorbed intermediates does not occur to an appreciable extent over this potential range. The results are substantive currents in potentiostatic 2-PrOH electro-oxidations over Pt, Ru, and Pt–Ru catalysts in base over this low potential range [7,9,10]. These facile kinetics at low anode potentials were also demonstrated in fuel cells. For example, in a Nafion®-based cell, the 2-PrOH fuel exhibited ~ 200 mV higher cell voltage at 80 mA cm^{-2} than MeOH fuel [11]. In a liquid KOH electrolyte cell, a higher open circuit voltage (OCV) was recorded for 2-PrOH fuel and up to 16 mA cm^{-2} the performance of the 2-PrOH cell was stable with potential cycling from OCV to 0.5 V while the MeOH cell performance degraded severely after three cycles [1]. This degradation was attributed to substantial poisoning in the presence of MeOH.

At moderate electrode potentials, however, acetone and other intermediates strongly adsorb to the Pt surface, slowing the 2-PrOH oxidation until they are removed at higher potentials where oxyhydroxide species form on the Pt surface (Equation (2)). This poisoning manifests itself as low-potential current maxima in potentiostatic 2-PrOH electro-oxidations [7,9,10], and as unstable, dropping cell voltages for 2-PrOH fuel cells at $E_{\text{cell}} < \sim 0.5$ V [12,13]. In summary, over the entire potential range, the major 2-PrOH oxidation product is acetone, whereas CO_2 is a minor product at higher potentials [8].

Previous work in our group showed that incorporation of Ru [7] and Ni [9,10] increases the stabilized, potentiostatic currents for the electro-oxidation of 2-PrOH over Pt. The enhancement over Pt–Ru occurs from low to high potentials, whereas Ni promotes the electro-oxidation at potentials above 250 mV vs. RHE. At high potentials, it appears that Ni promotes the electro-oxidation mainly by a bifunctional mechanism, where Ni provides oxygen-containing species to oxidize the strongly bound intermediates and form CO_2 .

In this study, we report the use of nanopillar Ni films deposited by glancing angle deposition (GLAD) as substrates for Pt electro-deposition. Comprehensive reviews of the GLAD technique have been reported previously [14,15]. In summary, GLAD is a physical vapour deposition (PVD) technique performed *in vacuo*, and is achieved by the precise motion of the substrate relative to the incoming vapour flux. The oblique deposition angle, denoted as α , is the angle between the incident vapour flux and substrate normal, and the angle of rotation about substrate normal is denoted as ϕ . These angles are shown schematically in Fig. 1a. A schematic of a GLAD apparatus in typical PVD system can be found

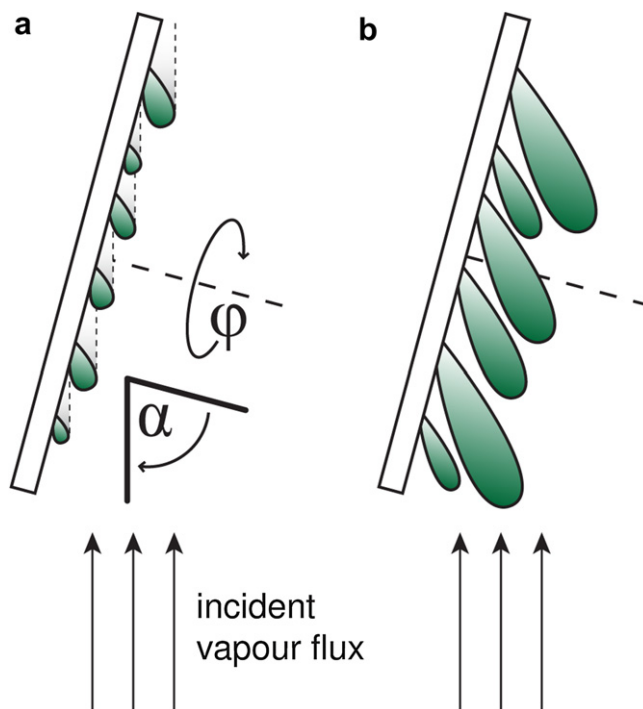


Fig. 1. (a) Schematic of the oblique deposition angle, α , and rotation angle about the substrate normal, ϕ , as defined in the GLAD process and (b) self-shadowing effect resulting in pillar-shaped growth.

in Figure 1.6 of Ref. [15]. During the deposition, the obliquely incident atoms are only able to nucleate onto the highest points of the surface due to a self-shadowing effect (Fig. 1a). With increasing flux deposition, this self-shadowing effect extends to columnar or pillar-shaped growth, as shown in Fig. 1b. Control over porosity and nanopillar spacing is achieved by changing the deposition angle α . Modulation of substrate rotation in ϕ adds further morphology control and access to various structures (e.g. vertical columns, slanted posts, chevrons, square spirals, helices, and combinations thereof).

The GLAD technique has been used for advanced nanostructuring in a variety of applications, including: nanoengineered optical thin films, such as square spiral photonic crystals [16] and antireflection coatings [17,18]; ordered small molecule organic photovoltaic bulk heterojunctions [19,20]; columnar microbattery electrodes [21]; and anisotropic ultrathin-layer chromatography plates [22]. The high level of morphology control inherent to GLAD leads to well-tailored nanostructures for each application.

GLAD-based nanostructures have been studied as electrocatalysts in fuel cells and related systems. For example, Bonakdar-pour et al. sputtered Pt onto high-surface area GLAD columnar Ti to prepare oxygen reduction electro-catalysts with a 10–15 times increase in electrochemical surface area compared to smooth Pt [23]. Khudhayer et al. also reported GLAD-fabricated nanostructures as catalysts for the oxygen reduction reaction (ORR) [24]. Their nanorod arrays of Pt on glassy carbon substrates have higher area-specific activity towards the ORR, as well as higher stability towards potential cycling in acid, than conventional Pt/C catalysts. In fact, the reported specific activity was similar to bulk polycrystalline Pt. This high area-specific activity was attributed to the large crystallite size and to the results of a crystallographic analysis that concluded that the nanorod sidewalls were dominated by Pt (110) planes. The mass-specific activity of the GLAD Pt deposits was lower than that of Pt/C. Gasda et al. incorporated GLAD Pt cathode catalyst layers onto gas diffusion layers and evaluated their

performance in fuel cells [25]. They demonstrated that the porosity control provided by the GLAD process allowed improvements to mass transport. As a result, electrodes made from GLAD Pt deposits had higher mass-specific activities than electrodes made from conventional Pt black at high current densities.

Although there are no reports of Pt–Ni electro-catalysts prepared by GLAD, the Dahn group has reported [26,27,28] related systems comprised of Pt and Ni co-deposits prepared by sputter deposition onto a nanostructured thin film (NSTF). The NSTF comprises high surface area, closely-packed crystalline 500–1000 nm long whiskers of vacuum annealed N,N-di(3,5-xylyl)perylene-3,4:9,10-bis(dicarboximide) fabricated by 3M [29]. It has been shown for related Pt-based deposits that the equilibrium shape and faceting of such deposits are whiskerettes, on the sides of the whiskers, comprised of polycrystalline layers with highly oriented crystallites with the (111) face predominantly exposed [29]. The ORR activity of a range of $\text{Pt}_{1-x}\text{Ni}_x$ ($0 \leq x \leq 1$) alloy deposits on NSTF was studied with rotating disk voltammetry in perchloric acid electrolytes and in a membrane electrode assembly (MEA). The predominant features of these systems are that Ni dealloys by dissolution during the ORR in acid, the dissolution initially increases the ORR activity of these catalysts to quite high levels by increasing the number of exposed Pt sites and by increasing the intrinsic activity of the exposed Pt, and systems with $x = 0.69 \pm 0.02$ have an extraordinarily sharp activity maximum upon dealloying of Ni. The dissolution of Ni into the membrane electrolyte, however, impedes the activity of H_2 /air fuel cells operating with these cathode catalysts.

Our GLAD Ni substrate consists of 500 nm GLAD Ni nanopillars (Ni_{NP}) deposited onto a planar Ni film. We electrochemically deposited low-mass loadings ($<0.3 \text{ mg cm}^{-2}$) of Pt onto the Ni_{NP} working electrode via two methods. The first was our previously reported, self-limiting, high current density galvanostatic deposition in 2 M NH_4Cl with a Pt counter electrode as the source of Pt [9]. We will refer to this as the counter electrode (CE) Pt deposition and the resulting deposit as $\text{Pt}_{\text{CENiNP}}$. The second deposition was a more traditional potentiostatic deposition [30] from K_2PtCl_6 in aqueous HClO_4 , to prepare a deposit we denote as $\text{Pt}_{\text{TrNiNP}}$. The pristine Ni_{NP} substrates, and $\text{Pt}_{\text{CENiNP}}$ and $\text{Pt}_{\text{TrNiNP}}$ catalysts were all characterised by Scanning Electron Microscopy (SEM), X-ray diffraction (XRD), X-ray Photoelectron Spectroscopy (XPS), Inductively Coupled Plasma-Mass Spectrometry (ICP-MS) and voltammetry. The potential of all materials were kept below $\sim 0.5 \text{ V}$ vs. RHE, and the electrochemical studies were carried out in base in order to minimize dissolution of Ni and obtain information about the surface as made by the deposition. Finally, the catalytic activities towards 2-PrOH electro-oxidation are measured and compared to a shiny Pt foil (Pt_{foil}), Pt deposited onto commercially-available Ni foam via the CE deposition ($\text{Pt}_{\text{CENiFoam}}$) [10], and commercially available Pt and Pt–Ru nanoparticles [10]. This is the first reported study of GLAD-based Pt–Ni catalysts and alcohol oxidation over GLAD-based electro-catalysts.

2. Experimental

2.1. Preparation of GLAD Ni substrates

Nanopillar Ni films were deposited by glancing angle deposition on Si substrates (p-type, (100), University Wafer). Si wafers were rinsed subsequently in acetone, isopropyl alcohol, and water before being diced into $1 \text{ cm} \times 2 \text{ cm}$ pieces. The samples were placed in a high vacuum deposition chamber (Kurt J. Lesker) that was evacuated to below 0.1 mPa. A 10 nm layer of Ti (1 inch target, 99.95%)

was sputtered at 75 W under Ar flow. The Ti layer promotes adhesion between the substrate and Ni layers. Ni was then deposited from Ni metal chunks (Cerac, Inc., 99.9%) via electron beam deposition. The flux rate was maintained at 1 nm s^{-1} while the substrate was rotated constantly in ϕ at a rate of one rotation every 10 nm of film growth. A 200 nm planar layer of Ni was first deposited at a deposition angle of $\alpha = 30^\circ$, followed by 500 nm of vertical nanopillars deposited at $\alpha = 85^\circ$. After GLAD deposition, a task wipe was used define a $1 \text{ cm} \times 1 \text{ cm}$ area of GLAD Ni nanopillars for deposition of Pt.

2.2. Preparation of Pt deposits

Both Pt depositions were performed using a Solartron SI 1287 Electrochemical Interface controlled with CorrWare for Windows Version 2-3d software. The deposition apparatus comprised a $10 \text{ cm} \times 2.5 \text{ cm}$ diameter glass cylinder equipped with a stir bar and an Aldrich Ag/AgCl double junction reference electrode. Before deposition, the 1 cm^2 Ni_{NP} substrates were washed gently with triply distilled water.

2.2.1. Counter electrode Pt deposition

The counter electrode used for the CE Pt deposition was a $25 \text{ mm} \times 25 \text{ mm}$ Pt gauze (Alfa Aesar, 99.9% metals basis) blackened with 0.02 M K_2PtCl_6 (Aithaca Chemical Corp.) in 1 M HClO_4 (Anachemia Corp.). A typical blackening experiment would be performed at -0.1 V vs. Ag/AgCl until the current decayed to $\sim 0 \text{ mA}$ ($\sim 36 \text{ min}$). The real surface area was determined based on the H_{UPD} (H_{UPD} = Hydrogen underpotential deposition) peak of a stabilised cyclic voltammogram (0 – 0.5 V , 1 mV s^{-1}) recorded in N_2 -purged 0.5 M H_2SO_4 assuming the charge associated with a monolayer of hydrides on polycrystalline Pt is $210 \mu\text{C cm}^{-2}$ [31] with 77% efficiency. The resulting surface areas were typically more than $25,000 \text{ cm}^2$. It is noted that each counter electrode was not used to deposit Pt on Ni_{NP} substrates more than 3 times without being freshly blackened.

The CE Pt deposition was performed by applying a constant current of -100 mA for 1 h between a Ni_{NP} working electrode (WE) and the blackened Pt gauze counter electrode (CE) in 30 mL of 2 M NH_4Cl (Caledon Laboratory Chemicals) stirred at 500 rpm. The WE was positioned with the nanopillar film facing the CE and the reference electrode was positioned as close to WE as possible without impeding the CE. The potential of the CE during deposition was monitored by a Radio Shack multimeter using Scope View version 1.08 software. After Pt deposition, the working electrodes were gently rinsed with copious amounts of triply distilled water and used immediately in electrochemical experiments, or dried in air and used for characterization. Inductively Coupled Plasma-Mass Spectrometry (ICP-MS) was used to determine the mass of Pt deposited on the substrate. The sample was dissolved in *aqua regia* and evaporated to dryness on a hot plate. The residue was then made up in 0.3 M HNO_3 (EMD Chemicals) and submitted for analysis. For a typical $\text{Pt}_{\text{CENiNP}}$ sample, the mass of Pt was $251 \mu\text{g}$ Pt, which is consistent with previous studies [9,10].

2.2.2. Traditional Pt deposition

The traditional Pt deposition was performed by applying a 20 min potential step of -100 mV vs. Ag/AgCl between the Ni_{NP} working electrode and a Pt counter electrode shielded from solution behind a porous glass frit in a glass tube. The electrolyte comprised 25 mL of an aqueous solution of $1.2 \times 10^{-4} \text{ M}$ K_2PtCl_6 (Aithaca Chemical Corporation) and 0.01 M HClO_4 (Anachemia Corporation) prepared by serial dilution stirred at 500 rpm. For a pristine $\text{Pt}_{\text{TrNiNP}}$ sample, $77 \mu\text{g}$ Pt was detected by ICP-MS.

2.3. Characterisation and activity of electrodes

SEM was used to image the morphology of the substrates and catalysts with a Hitachi S-4800 instrument. Where side images were necessary, the samples were first cleaved before mounting to SEM stubs. XRD was performed on an Inel diffractometer equipped with a CPS 120 detector. Reference XRD patterns were generated using Powdercell 2.3 freeware.

A Kratos Analytical Axis Ultra X-ray Imaging Photoelectron Spectrometer was used to run XPS. Data fitting was performed using CasaXPS Version 2.3.16 software. The spectra were calibrated to adventitious carbon at 284.8 eV. The binding energies of the component peaks were calculated from the background-subtracted spectrum using an applied Shirley background. All peaks were fit with 30% Gaussian–Lorentzian curves whereas metallic components were additionally assigned 10–11% asymmetry in their higher binding energy tails. The intensity ratios of the Pt 4f_{7/2} and 4f_{5/2} peaks were set to the theoretical value of 4:3 and spin-orbit coupling was 3.3 eV; the Ni 3p_{3/2} and 3p_{1/2} peaks intensity ratio was 2:1 and separated by 1.9 eV. Reference data was retrieved from the National Institute of Standards and Technology (NIST) XPS online database [32].

Electrochemical measurements were collected on the same Solartron SI 1287 Electrochemical Interface used for the Pt depositions and investigated using a three-electrode cell with a static reversible hydrogen electrode (RHE). All potentials quoted are versus this reference unless otherwise stated. The prepared electrodes (Ni_{NP}, Pt_{CE}Ni_{NP} and Pt_{TR}Ni_{NP}) were used as working electrodes. A shiny Pt foil or blackened Pt gauze isolated behind a glass tube with a porous glass frit was used as a counter electrode.

All electrolytes were prepared using triply distilled water and analytical grade reagents. Electrolytes were purged with pre-purified N₂ gas (Praxair) before use, and all experiments were carried out under N₂. Cyclic voltammetry was performed at 25 °C in 1 M KOH. Electro-catalytic activity was recorded at 60 °C in 1 M solutions of KOH (Caledon Laboratory Chemicals) and (CH₃)₂COH (Sigma–Aldrich) in water. The (CH₃)₂COH was freshly distilled before use, and the cell was equipped with a dry ice/acetone condenser to minimize loss of the alcohol by evaporation. Sampled current voltammograms were constructed by plotting the steady state current at the end of 15 min potentiostatic oxidations against the potential. Prior to stepping to the desired potential, the working electrode was held at a constant potential of 0 mV for 1 min. The shiny Pt foil electrode used as an activity comparison was 0.8 cm × 1.7 cm, for a total geometric area in contact with the electrolyte and fuel of ~2.7 cm².

3. Results and discussion

Fig. 2a and b show the voltage and current responses recorded during representative depositions of Pt_{CE}Ni_{NP} and Pt_{TR}Ni_{NP}, respectively. The main differences in the conditions of these depositions are outlined in Table 1. Compared to our previous reports [9,10], the CE Pt deposition behaved as expected, that is, H₂ evolution was observed with a rise in the potential of the WE. This behaviour occurs because the overpotential for H₂ evolution over Ni is high under these conditions, but not over Pt, causing the potential of the electrode and the amount of H₂ evolution to increase as Pt is deposited on the Ni surface. The WE potential observed therefore represents a mixed-potential condition at the Ni and newly deposited Pt surfaces. The counter electrode potential was steady at ~1.1 V vs. Ag/AgCl for the duration of the experiment. The amount of Pt dissolved into solution is limited by self-passivation of the counter electrode under these conditions [33]. The traditional deposition also occurred as expected [30]. The

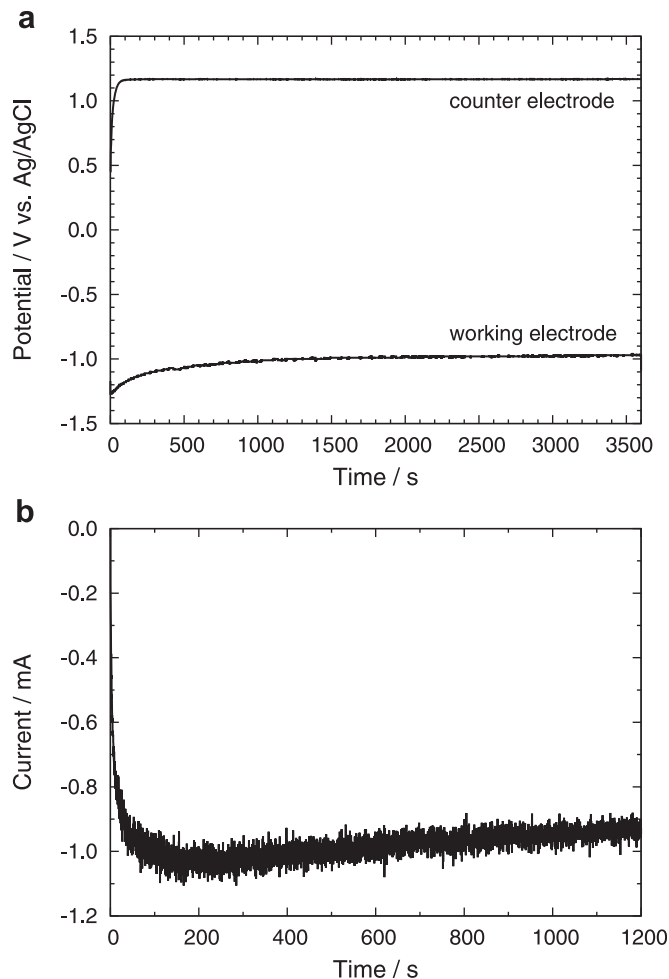


Fig. 2. (a) Potential profiles of the electrodes during the unconventional galvanostatic deposition of Pt_{CE}Ni_{NP} at -100 mA for 1 h in 2.0 M NH₄Cl. (b) Current profile of the traditional potentiostatic deposition of Pt_{TR}Ni_{NP} at 100 mV vs. Ag/AgCl in 0.006 wt% K₂PtCl₆ in 0.01 M HClO₄.

pale yellow colour of the solution faded and the current held constant at ~-1 mA for the duration of the experiment.

Fig. 3 shows SEM images of the Ni_{NP}, Pt_{CE}Ni_{NP} and Pt_{TR}Ni_{NP}. The Ni_{NP} (Fig. 3a and d) grew as columnar pillars that are perpendicular to the substrate surface and that widen with increasing height. The average pillar diameter is ~200 nm at the maximum height of ~500 nm. The number density is ~15 μm⁻². These dimensions correspond to a roughness factor of ~5 in the approximation of smooth cylindrical pillars. The SEM images also show that the Ni nanopillar film is composed of smaller, vertically oriented, and

Table 1
Comparison of the conditions for the Pt depositions employed herein.

	Pt counter electrode deposition	Traditional Pt deposition
Type of deposition	Galvanostatic, -100 mA	Potentiostatic -100 mV vs. Ag/AgCl
Electrolyte	2 M NH ₄ Cl; bulk pH ~5	0.01 M HClO ₄ ; bulk pH ~2
Source of Pt	Dissolution of blacked Pt gauze counter electrode	Added to solution as K ₂ PtCl ₆
Conditions at working electrode	Reducing conditions ~-1.2 V vs. Ag/AgCl	Less reducing conditions -0.1 V vs. Ag/AgCl

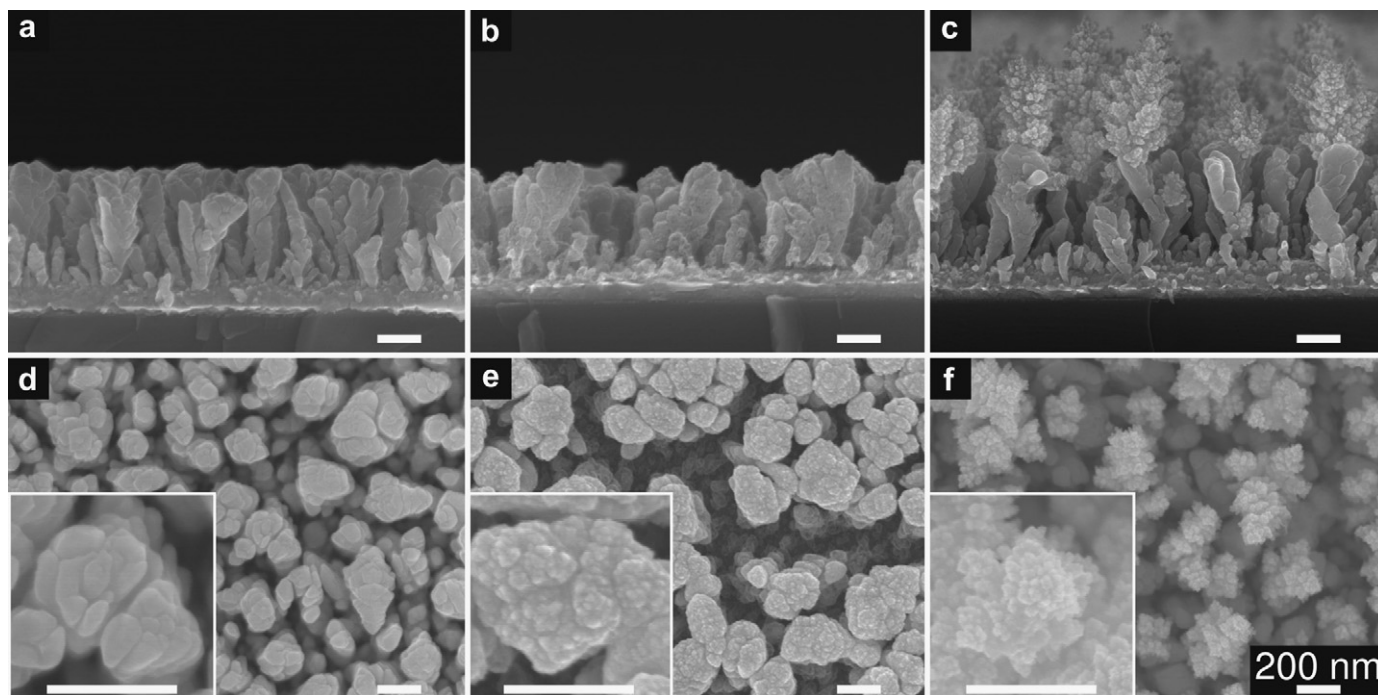


Fig. 3. Scanning Electron Micrographs showing cross-sectional views of (a) Ni_{NP} , (b) $\text{Pt}_{\text{CE}}\text{Ni}_{\text{NP}}$ and (c) $\text{Pt}_{\text{Tt}}\text{Ni}_{\text{NP}}$ and plan views of the same (d), (e) and (f) respectively. All scale bars represent 200 nm.

elongated pillar-shaped grains. The tops of the pillars appear segmented into the tops of the grains. The nanopillar Ni films do not have perfectly smooth surfaces (Fig. 3a and d), and all nodules, crevices, and grains contribute to a higher actual roughness than the approximated factor of ~ 5 .

Fig. 3b and e show the side and plan view of the Ni_{NP} after the CE Pt deposition. The Ni_{NP} are largely intact after the CE Pt deposition, and the underlying structure is visible under the Pt deposit. The Ni_{NP} do show slight wilting together, as is typical of GLAD films after solution processing and drying (Fig. 3e [34]). The tops and sides of the nanopillars were roughened by the CE Pt deposition, showing that Pt was deposited over the entire nanopillar surface. This result is consistent with the self-limiting nature of the CE Pt deposition we observed previously for Ni gauze and foam substrates [9,10]. We believe that the combination of the aforementioned mixed potential Pt–Ni surface, and the facile evolution of H_2 over Pt, results in a preferential deposition of Pt onto Ni until a thin layer of Pt forms on the Ni_{NP} surface.

In stark contrast, there is a distinct region of Pt growth by the traditional deposition (Fig. 3c and f). In this case, Pt nucleation and growth occurs predominantly on top of each Ni nanopillar, as a ~ 500 nm rough, Pt extension that resembles lilac flowers. The traditional Pt deposition appears to be mass-transport limited, that is, nucleation occurs as Pt arrives at the most exposed (top) surface of the pillars. Subsequently, the majority of growth processes occurs at the Pt deposits on the top of the pillars.

Fig. 4 shows the XRD diffractograms obtained from the Ni_{NP} , $\text{Pt}_{\text{CE}}\text{Ni}_{\text{NP}}$, and $\text{Pt}_{\text{Tt}}\text{Ni}_{\text{NP}}$ materials. The XRD data show that the diffracting portion of the Ni_{NP} consists of polycrystalline Ni in the fcc phase. The hcp phase was not detected. The Scherrer Ni grain diameter (calculated from the Ni (111) peaks of 13 samples) was 35 ± 8 nm. This dimension roughly corresponds to those of the smaller, vertically oriented, and elongated column-shaped grains observed in the SEM images of the Ni nanopillars (Fig. 3). The relative intensities of the Ni (200), (220), and (311) peaks in all three samples are less intense than those in bulk, polycrystalline Ni.

Expressed differently, the relative intensities of the Ni (111) and (222) peaks are higher than those in bulk, polycrystalline Ni. These relative intensities suggest that the {111} family of planes are preferentially oriented in the GLAD Ni_{NP} samples, regardless of whether Pt has been deposited. No alloying is detectable between the Ni and Pt, as the position of the Ni peaks in Ni_{NP} (Fig. 4a) is superimposable onto both of the Pt-containing samples (Fig. 4b and c).

The diffractograms for both $\text{Pt}_{\text{CE}}\text{Ni}_{\text{NP}}$ and $\text{Pt}_{\text{Tt}}\text{Ni}_{\text{NP}}$ display peaks for Pt in the fcc phase. For the $\text{Pt}_{\text{Tt}}\text{Ni}_{\text{NP}}$ sample, the relative intensities of the Pt (200), (220) and (311) peaks are slightly less than those in bulk, polycrystalline Pt, but the (222) peak is more intense than expected. These relative intensities suggest that Pt growth proceeds with a preferential orientation of the {111} family of planes.

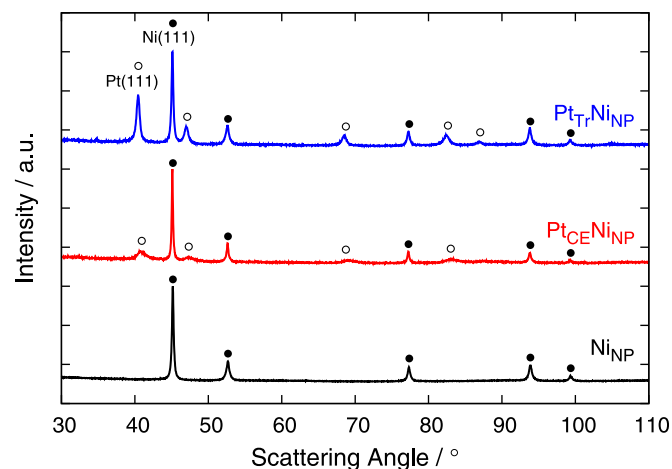


Fig. 4. X-ray diffraction patterns of Ni_{NP} , $\text{Pt}_{\text{CE}}\text{Ni}_{\text{NP}}$ and $\text{Pt}_{\text{Tt}}\text{Ni}_{\text{NP}}$. Ni peaks are denoted by filled circles and Pt peaks are denoted by unfilled circles.

The relative Pt:Ni peak intensities for the Pt_{Tr}Ni_{NP} sample is much higher than for the Pt_{CE}Ni_{NP} sample, and the full width at half maximum is perhaps narrower, showing that the traditional deposition forms larger amounts of polycrystalline Pt than the CE Pt deposition. This is consistent with the results of the SEM studies (Fig. 3) showing the conformal nature of the CE Pt deposition. The Scherrer Pt grain diameter (calculated from the Pt (111) peak) for the Pt_{CE}Ni_{NP} samples was on average 9 ± 2 nm (3 samples), whereas for Pt_{Tr}Ni_{NP}, the typical diameters were 10 ± 4 nm (5 samples). These relatively small Pt grain sizes were promising as the first aim of this study was to create deposits with relatively large surface areas.

Fig. 5 shows the stabilized cyclic voltammograms (CVs) for the Ni_{NP}, Pt_{CE}Ni_{NP}, and Pt_{Tr}Ni_{NP} materials in 1 M KOH at room temperature. The CVs in Fig. 5a were recorded with lower (−0.1 V) and upper (0.4 V) potential limits that are typically employed for Ni in base [9,10], and are normalized to the geometric area of the nanopillars, i.e. 1 cm². The results show that the Ni_{NP} is substantially more active towards H₂ evolution than Ni_{black} (Inset of Fig. 5a, reproduced from Ref. [10]). Although the origins of this difference are unknown, it is a reproducible phenomenon that likely arises from structural features of the GLAD Ni_{NP}. In Fig. 5a, the shapes of both the Pt_{CE}Ni_{NP} and the Pt_{Tr}Ni_{NP} are similar to our previous report of a CE Pt deposition on Ni foam at the same potential range (Fig. 4b

in Ref. [10]). Also, the PtNi_{NP} deposits are more efficient at H₂ production than Ni_{NP} alone, with significant peaks for H₂ production and oxidation in the cathodic and anodic scans over Pt_{CE}Ni_{NP} and Pt_{Tr}Ni_{NP}.

The lower potential limit was varied to minimize the effects of H₂ evolution. Fig. 5b shows the resulting CVs. The α -Ni(OH)₂ peak appears to be present in the cathodic scan of the Ni_{NP} CV at $E_{\text{peak}} \sim 0.06$ V, but the corresponding anodic peak ($E_{\text{peak}} \sim 0.22$ V) is broad and not well defined, as compared to Ni_{black} (Inset Fig. 5a). The origins of these differences require further investigation, but are likely connected to pre-polarization of the electrode [35,36]. The anodic charge of the α -Ni(OH)₂ peak is proposed to be an estimate of the surface area of Ni electrodes where $Q = 514 \mu\text{C cm}^{-2}$ [37], although work in this group using destructive CO stripping experiments show that this number likely underestimates the surface area by a factor of ~ 2.6 [9]. The charge under the α -Ni(OH)₂ anodic peak in the CV of Ni_{NP} corresponds to a surface area of $20.5 \text{ cm}^2 \text{ cm}^{-2}$. We consider this value to be only a tentative, lower limit to the real surface area of the Ni_{NP}.

The CVs of Pt_{CE}Ni_{NP} and Pt_{Tr}Ni_{NP} in Fig. 5b contain features that are associated with those of Pt, with the apparent surface area of the Pt_{CE}Ni_{NP} being larger than Pt_{Tr}Ni_{NP} and Ni_{NP}. Both CVs have features associated with hydrogen adsorption in the cathodic sweeps, and peaks for oxidation of adsorbed hydrogen in the anodic sweeps. If we treat the CVs as polycrystalline Pt (that is, no Ni component present) the estimated surface areas from the charge associated with H_{UPD} are 32.0 and $23.3 \text{ cm}^2 \text{ cm}^{-2}$ respectively for Pt_{CE}Ni_{NP} and Pt_{Tr}Ni_{NP}.

The activity of the Ni_{NP}, Pt_{CE}Ni_{NP} and Pt_{Tr}Ni_{NP} catalysts towards 2-propanol oxidation in base was measured and compared to the activity of a shiny Pt foil (Pt_{foil}). Fig. 6a shows a comparison of the sampled current voltammograms (SCVs) of the different catalysts based on their respective geometric areas. The catalysts were reduced at 0 V for 60 s, and then stepped to the desired potential. The steady-state currents were sampled after 15 min. All the samples exhibited the low-potential current maximum associated with partial 2-propanol oxidation followed by acetone inhibition (50–300 mV vs. RHE). It appears that the high activity of Pt_{Tr}Ni_{NP} at low potentials is a summation of the activity of the Pt and Ni deposits (*vide infra*). Above 300 mV, the Ni_{NP} electrode was the only catalyst that did not show any activity, while the bimetallic catalysts demonstrated significantly higher activity, with the CE Pt deposited catalyst performing the best.

Fig. 6b shows a comparison of the SCVs normalized by the estimated number of surface atoms. We include the activities of unsupported Pt and Pt–Ru nanoparticles (Johnson–Matthey HiSPECTM 1000 and HiSPEC 6000) [7] and a Pt_{CE}Ni_{foam} electrocatalyst we prepared by Pt CE deposition onto a commercially-available Ni foam substrate [10]. The number of surface atoms on the Pt_{CE}Ni_{NP} and Pt_{Tr}Ni_{NP} catalysts was estimated from the charge in the H_{UPD} region of the respective cyclic voltammograms recorded in base (Fig. 5b). The figure shows that the normalized activity of Pt_{CE}Ni_{NP} was higher than both Pt_{CE}Ni_{foam} and unsupported Pt nanoparticles at low and high potentials. The low-potential peak currents for the Pt_{CE}Ni_{NP} and the unsupported Pt–Ru catalysts were comparable, while Pt_{CE}Ni_{NP} appeared more active at potentials greater than 450 mV. Pt_{Tr}Ni_{NP} was the most active at low potentials, but was less active than Pt_{CE}Ni_{NP} at high potentials.

To explain the activity of Ni_{NP} at low potentials but not at high potentials, two hypotheses were tested. The first hypothesis was that Ni_{NP} are not active towards 2-PrOH oxidation, therefore the current density observed below 300 mV is as a result of oxidation of the Ni_{NP} surface (Equation (4)).

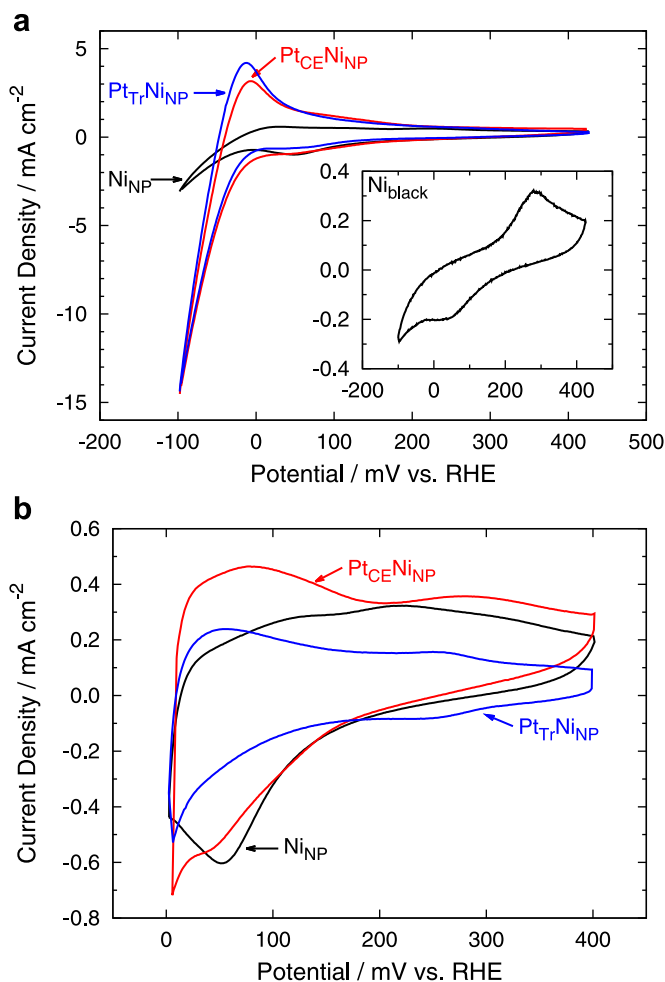


Fig. 5. Cyclic voltammograms of Ni_{NP} (black), Pt_{CE}Ni_{NP} (red) and Pt_{Tr}Ni_{NP} (blue) in 1 M KOH at 25 °C with a scan rate of 10 mV s^{-1} . (a) Potential range: −100 to 425 mV; Inset Ni_{black}. (b) Potential range: 0–400 mV. (For interpretation of the references to colour in this figure legend, the reader is referred to the web version of this article.)

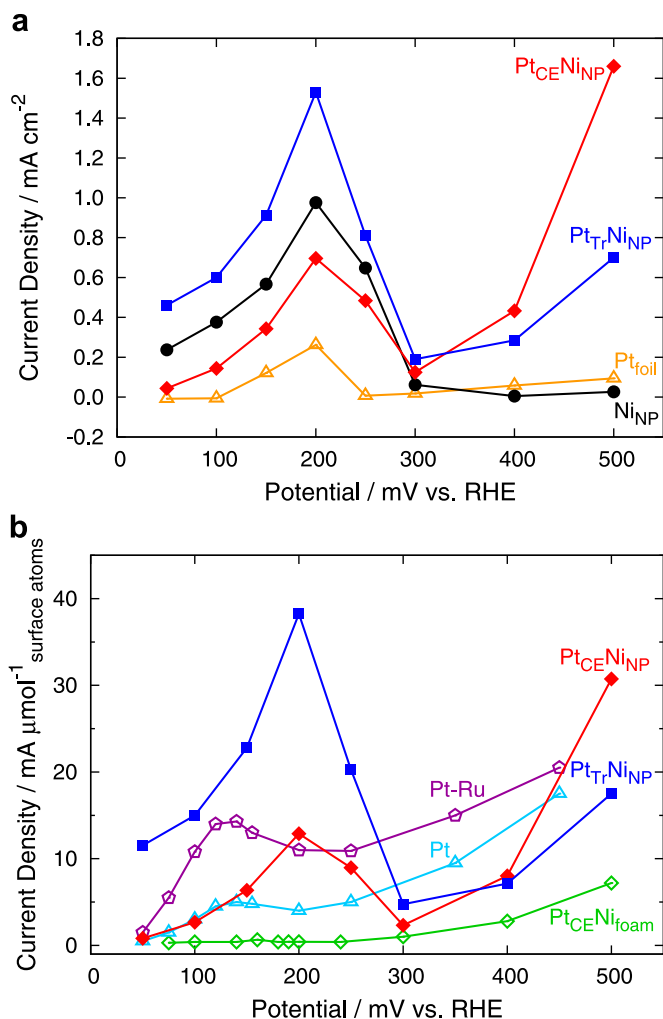


Fig. 6. (a) Sampled current voltammograms of NiNP (black circles), PtCENiNP (red diamonds), PtTfNiNP (blue squares) and Ptfoil (orange open triangles) in 1 M KOH + 1 M (CH₃)₂COH at 60 °C. The steady-state current after the catalysts are polarized for 15 min is plotted against the potential of the step. The current densities are based on the geometric area of the catalysts (1 cm² for all GLAD Ni-based electrodes and 2.7 cm² for the Pt foil). (b) Sampled current voltammograms for the oxidation of 2-propanol in base at 60 °C normalized by the estimated number of surface atoms. Note that PtCENiNP (red diamonds) and PtTfNiNP (blue squares) are in 1 M KOH + 1 M (CH₃)₂COH, PtCENi_{foam} (green open diamonds) [10] is in 0.5 M NaOH + 1 M (CH₃)₂COH, and Pt nanoparticles (teal open triangles) and Pt–Ru nanoparticles (purple open pentagons) [7] are in 1 M NaOH + 1 M (CH₃)₂COH. (For interpretation of the references to colour in this figure legend, the reader is referred to the web version of this article.)

As a control experiment, the same potentiostatic procedure was replicated in alcohol-free electrolyte. The results show that the current density between 50 and 300 mV in the 2-PrOH-free electrolyte was lower than when the alcohol was present, but not negligible (Fig. 7). The anodic current observed in the presence of 2-PrOH below 300 mV is therefore a combination of surface oxidation and alcohol oxidation.

The second hypothesis was that the potentiostatic experiments performed below 300 mV collectively oxidise the NiNP electrodes to the point of surface passivation before activity above 300 mV could be recorded. Hence, as a control, the potential steps were carried out from 300 to 500 mV first and then from 50 to 250 mV. The SCV in Fig. 7 shows that the low potential current maximum is still present and there is no oxidation activity above 300 mV, meaning that NiNP is oxidised but not passivated above 300 mV.

Together, these results are evidence that Ni nanopillars are active towards 2-PrOH oxidation below 300 mV, but not above

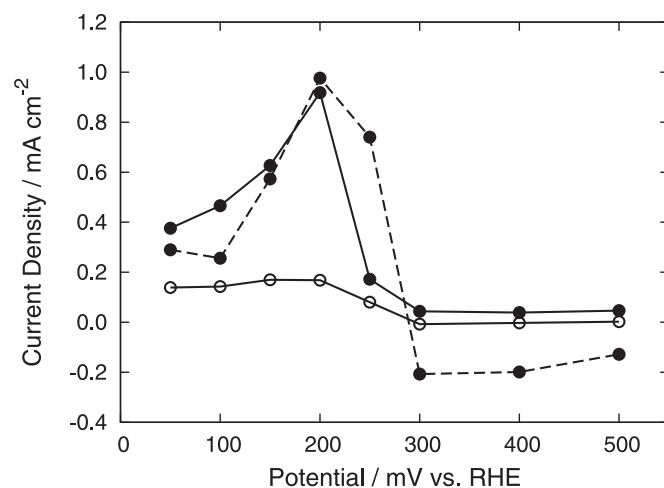


Fig. 7. Sampled current voltammograms of NiNP in 1 M KOH at 25 °C (unfilled circles), in 1 M KOH + 1 M (CH₃)₂COH at 60 °C (solid line, filled circles), and in 1 M KOH + 1 M (CH₃)₂COH at 60 °C with data collected from 300–500 mV then 50–250 mV (dashed line, filled circles). The steady-state current after the catalysts are potentiostated for 15 min is plotted against the potential of the step. The current densities are based on the geometric area of the catalysts (1 cm²).

300 mV. It follows that the activities of the PtCENiNP and PtTfNiNP catalysts below 300 mV result from combinations of the activity of the Pt and Ni components. Above 300 mV, the Ni component in both catalysts is oxidised but not passivated, therefore a bifunctional mechanism could be induced. Park et al. have described this behaviour for MeOH oxidation over Ni–Pt catalysts [38,39]. The authors suggest that oxides on Ni act as oxygen donors in a surface redox process that removes CO poisons during MeOH oxidation at long times. An analogous process likely occurs during the oxidation of adsorbed acetone and related species at higher potentials over PtCENiNP. Such a bifunctional process is expected to be less prevalent over PtTfNiNP because there is less contact between the Ni and Pt surfaces, and accounts for its lowered relative activity above 300 mV. However, this analysis does not rule out any possible electronic effects in either catalyst.

XPS was performed to probe any electronic effects that could contribute to the activity difference observed between PtCENiNP and PtTfNiNP catalysts. Fig. 8 shows the Pt 4f XPS spectra collected on PtCENiNP and PtTfNiNP. Both spectra display a doublet of metallic Pt peaks. Similar to our previous report, the PtCENiNP exhibits a Ni 3p shoulder at ~68 eV [10]. In contrast, this feature is absent for the PtTfNiNP catalyst. This is likely due to the thick (~500 nm) Pt layer observed in the PtTfNiNP SEM (Fig. 3c). The XPS probe depth is only ~3–9 nm therefore Ni was not strongly detected in this sample. Table 2 summarises the peak positions of the component peaks in the XPS spectra. No electronic shifts were observed for the PtCENiNP catalyst and a negligible +0.2 eV shift was observed for PtTfNiNP. Therefore, both catalysts are electronically similar to Pt and to each other.

We cannot discount the possibility that the activity of PtTfNiNP is higher than PtCENiNP at low potentials due to a geometric/composition effect as the major difference between the two bimetallic catalysts is the distribution of Pt on the surface. This geometric/composition effect has been described by Yang et al. for MeOH oxidation over bi-metallic catalysts [40] and well established by Gasteiger, Markovic, Ross and Cairns [41,42]. At least three neighbouring Pt sites in the correct crystallographic arrangement are required to activate MeOH chemisorption. If this mechanism is relevant for 2-PrOH, then the probability of having enough Pt sites in the correct orientation for 2-PrOH adsorption is higher in PtTfNiNP where the Pt is segregated to just the top of the posts. In

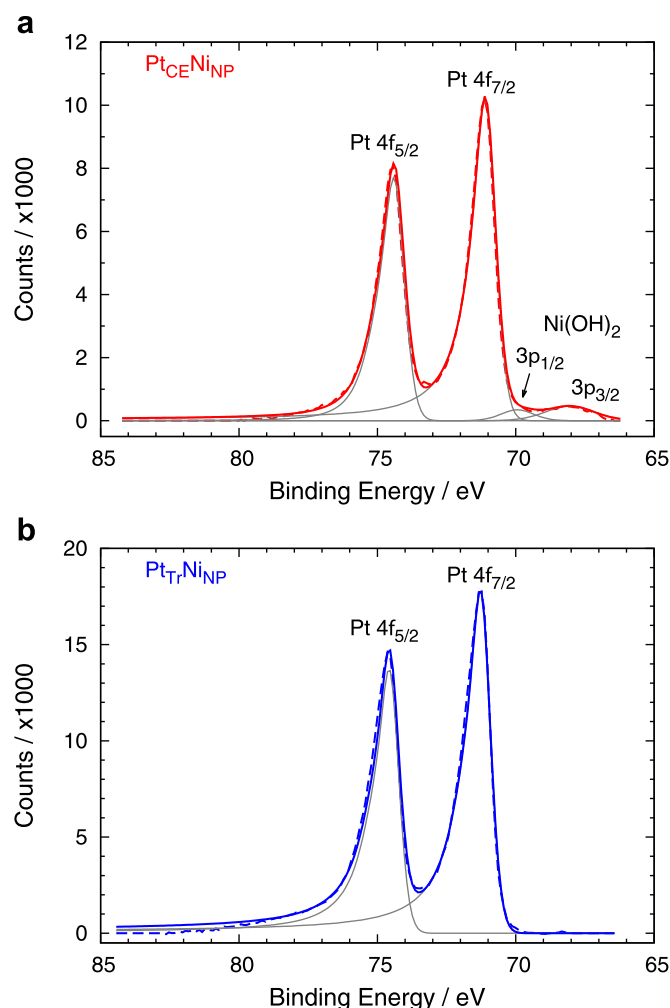


Fig. 8. X-ray photoelectron spectroscopy of (a) $\text{Pt}_{\text{CeNiNP}}$ and (b) $\text{Pt}_{\text{TiNiNP}}$. Dashed lines are experimental data, solid lines are calculated fits and solid grey lines are component peaks of the calculated fits.

Table 2

Reference and calculated binding energies and standard deviations used in XPS analysis of the catalysts.

Chemical state and spectral line	Binding energy (eV)		
	Reference	$\text{Pt}_{\text{CeNiNP}}$	$\text{Pt}_{\text{TiNiNP}}$
Pt $4f_{7/2}$	71.1 (0.1) ^a	71.1	71.3
Ni(OH) ₂ $3p_{3/2}$	68.0 (–)	68.0	–

^a Numbers in brackets denote the standard deviation for the values in the reference column. In all other columns experimental error was ± 0.1 eV. Dashes in brackets signify that no standard deviation has been recorded as only one value has been reported.

contrast, in $\text{Pt}_{\text{CeNiNP}}$, the Pt is homogeneously distributed and the likelihood of the correct arrangement for 2-PrOH adsorption is less favoured. This possible interpretation requires further investigation.

4. Conclusions

Herein we have reported the first alcohol oxidation study over GLAD-based catalysts. Bimetallic Ni–Pt electrodes were prepared via two methods: an unconventional self-limiting, galvanostatic Pt

deposition and a traditional potentiostatic deposition. Both methods were successful in incorporating Pt onto the surface of GLAD Ni nanopillars to effect an increase in electro-active surface area. Both catalysts showed superior activity towards 2-PrOH oxidation in base relative to a Pt_{foil} and $\text{Pt}_{\text{CeNiNP}}$. The normalized activity of $\text{Pt}_{\text{CeNiNP}}$ was higher than unsupported Pt nanoparticles at low and high potentials, while at low-potentials $\text{Pt}_{\text{CeNiNP}}$ was comparable to Pt–Ru; the normalized activity of $\text{Pt}_{\text{TiNiNP}}$ was superior below 300 mV. It was demonstrated that the GLAD Ni nanopillars themselves electro-oxidised 2-PrOH at potentials below 300 mV vs. RHE, therefore activity enhancement at low potentials was attributed to the combined activity of the Pt and Ni components in the catalysts. At potentials above 300 mV, a bifunctional mechanism was suggested where $\text{Pt}_{\text{CeNiNP}}$ experienced a higher bifunctional effect than $\text{Pt}_{\text{TiNiNP}}$. Overall, the results suggest that an optimum fuel cell catalyst made from these systems would be a combination of $\text{Pt}_{\text{CeNiNP}}$ and $\text{Pt}_{\text{TiNiNP}}$. Future work in our laboratories involves evaluating these catalysts towards the oxygen reduction reaction.

Acknowledgements

We thank the University of Alberta, the Natural Sciences and Engineering Research Council, Micralyne, and Alberta Innovates: Technology Futures for supporting this research. We also acknowledge GeoChem technician Guangcheng Chen of the Earth and Atmospheric Sciences Department for ICP-MS data collection, and Dr. Dimitre Karpuzov, Facility Manager at the Alberta Centre for Surface Engineering and Science for performing the XPS analysis. Finally, we recognise Brent Rudyk for assistance with processing the XPS results.

References

- [1] M.E.P. Markiewicz, S.H. Bergens, J. Power Sources 195 (2010) 7196–7201.
- [2] C. Lamy, A. Lima, V. LeRhun, F. Delime, C. Coutanceau, J. Léger, J. Power Sources 105 (2002) 283–296.
- [3] J.R. Varcoe, R.C.T. Slade, Fuel Cells 5 (2005) 187–200.
- [4] V. Bambagioni, C. Bianchini, A. Marchionni, J. Filippi, F. Vizza, J. Teddy, P. Serp, M. Zhiani, J. Power Sources 190 (2009) 241–251.
- [5] E. Bingham, B. Cohnsen, C.H. Powell, Patty's Toxicology (2011). Available at: http://knovel.com/web/portal/browse/display?_EXT_KNOVEL_DISPLAY_bookid=706&VerticalID=0 (accessed 11.10.11).
- [6] T. Kobayashi, J. Otomo, C. Wen, H. Takahashi, J. Power Sources 124 (2003) 34–39.
- [7] M.E.P. Markiewicz, S.H. Bergens, J. Power Sources 185 (2008) 222–225.
- [8] M.E.P. Markiewicz, D.M. Hebert, S.H. Bergens, J. Power Sources 161 (2006) 761–767.
- [9] L.N. Menard, S.H. Bergens, J. Power Sources 194 (2009) 298–302.
- [10] S.A. Francis, S.H. Bergens, J. Power Sources 196 (2011) 7470–7480.
- [11] Z. Qi, M. Hollett, A. Attia, A. Kaufman, Electrochem. Solid State Lett. 5 (2002) A129–A130.
- [12] Z. Qi, A. Kaufman, J. Power Sources 118 (2003) 54–60.
- [13] D. Cao, S.H. Bergens, J. Power Sources 124 (2003) 12–17.
- [14] M.M. Hawkeye, M.J. Brett, J. Vac. Sci. Technol. A 25 (2007) 1317–1335.
- [15] M.T. Taschuk, M.M. Hawkeye, M.J. Brett, Chapter 13–Glancing angle deposition, in: Peter M. Martin (Ed.), Handbook of Deposition Technologies for Films and Coatings, third ed., William Andrew Publishing, Boston, 2010, pp. 621–678.
- [16] M.A. Summers, K. Tabunshchik, A. Kovalenko, M.J. Brett, Photonic Nanostruct. Fundamentals and Applications 7 (2009) 76–84.
- [17] S. Kennedy, M.J. Brett, Appl. Opt. 42 (2003) 4573–4579.
- [18] J.Q. Xi, M.F. Schubert, J.K. Kim, E.F. Schubert, M. Chen, S.Y. Lin, W. Liu, J.A. Smart, Nat. Photon. 1 (2007) 176–179.
- [19] J.G. Van Dijken, M.D. Fleischauer, M.J. Brett, Org. Electron. 12 (2011) 2111–2119.
- [20] N. Li, S.R. Forrest, Appl. Phys. Lett. 95 (2009) 123309–123311.
- [21] M.D. Fleischauer, J. Li, M.J. Brett, J. Electrochem. Soc. 156 (2009) A33–A36.
- [22] S.R. Jim, M.T. Taschuk, G.E. Morlock, L.W. Bezuidenhout, W. Schwab, M.J. Brett, Anal. Chem. 82 (2010) 5349–5356.
- [23] A. Bonakdarpour, M.D. Fleischauer, M.J. Brett, J.R. Dahn, Appl. Catal. A 349 (2008) 110–115.
- [24] W.J. Khudhayer, N.N. Kariuki, X. Wang, D.J. Myers, A.U. Shaikh, T. Karabacak, J. Electrochem. Soc. 158 (2011) B1029–B1041.

- [25] M.D. Gasda, R. Teki, T.-M. Lu, N. Koratkar, G.A. Eisman, D. Gall, J. Electrochem. Soc. 156 (2009) B614–B619.
- [26] M.K. Debe, A.J. Steinbach, G.D. Vernstrom, S.M. Hendricks, M.J. Kurkowski, R.T. Atanasoski, P. Kadera, D.A. Stevens, R.J. Sanderson, E. Marvel, J.R. Dahn, ECS Trans. 33 (2010) 143–152.
- [27] C.K.G. Liu, D.A. Stevens, J.C. Burns, R.J. Sanderson, G. Vernstrom, R.T. Atanasoski, M.K. Debe, J.R. Dahn, J. Electrochem. Soc. 158 (2011) B919–B926.
- [28] D.A. Stevens, R. Mehrotra, R.J. Sanderson, G.D. Vernstrom, R.T. Atanasoski, M.K. Debe, J.R. Dahn, J. Electrochem. Soc. 158 (2011) B905–B909.
- [29] L. Gancs, T. Kobayashi, M.K. Debe, R. Atanasoski, A. Wieckowski, Chem. Mater. 20 (2008) 2444–2454.
- [30] A.M. Feltham, M. Spiro, Chem. Rev. 71 (1971) 177–193.
- [31] B.E. Conway, H. Angerstein-Kozłowska, Acc. Chem. Res. 14 (1981) 49–56.
- [32] C.D. Wagner, A.V. Naumkin, A. Kraut-Vass, J.W. Allison, C.J. Powell, J.R. Rumble Jr., NIST X-ray Photoelectron Spectroscopy Database, Version 3.5 (Web Version) (2003). Available at: srdata.nist.gov/xps (accessed 01.03.12).
- [33] Y. Xu, M. Shao, M. Mavrikakis, R.R. Adzic, in: A. Wieckowski, M.T.M. Koper (Eds.), Fuel Cell Catalysis-A Surface Science Approach, John Wiley and Sons, New Jersey, 2009, pp. 271–315.
- [34] J.K. Kwan, J.C. Sit, Nanotechnology 21 (2010) 1–6.
- [35] A. Seghioer, J. Chevalet, A. Barhoun, F. Lantelme, J. Electroanal. Chem. 442 (1998) 113–123.
- [36] S.A.S. Machado, L.A. Avaca, Electrochim. Acta 39 (1994) 1385–1391.
- [37] I.J. Brown, S. Sotiropoulos, J. Appl. Electrochem. 30 (2000) 107–111.
- [38] K.W. Park, J.H. Choi, B.K. Kwon, S.A. Lee, Y.E. Sung, H.Y. Ha, S.A. Hong, H. Kim, A. Wieckowski, J. Phys. Chem. B 106 (2002) 1869–1877.
- [39] K.W. Park, J.H. Choi, Y.E. Sung, J. Phys. Chem. B 107 (2003) 5851–5856.
- [40] H. Yang, C. Coutanceau, J. Léger, N. Alonso-Vante, C. Lamy, J. Electroanal. Chem. 576 (2005) 305–313.
- [41] H.A. Gasteiger, N. Markovic, P.N. Ross Jr., E.J. Cairns, J. Electrochem. Soc. 141 (1994) 1795–1803.
- [42] N.M. Marković, P.N. Ross Jr., Surf. Sci. Rep. 45 (2002) 117–229.